Check for updates

Advanced Engineering Materials

ADVANCED ENGINEERING MATERIALS
www.aem-journal.com

RESEARCH ARTICLE

Flash Roasting of ZnS: A Method to Produce Defect-Engineered ZnO

Pranav Rai[1,2] | Kumar Sadanand Arya[1] | Chandraprakash Singh[3] | Ravi Kumar[1,2,4,5]

[1]Laboratory for High Performance Ceramics, Department of Metallurgical and Materials Engineering, Indian Institute of Technology Madras (IIT Madras), Chennai, Tamil Nadu, India | [2]Rishi and Jyotsna Raj (RJR) Centre for Electrification of Materials Manufacturing, Indian Institute of Technology Madras (IIT Madras), Chennai, Tamil Nadu, India | [3]Department of Electronics and Communication Engineering, Indian Institute of Information Technology Ranchi, Ranchi, Jharkhand, India | [4]Research Centre on Ceramic Technologies for Futuristic Mobility, Indian Institute of Technology Madras (IIT Madras), Chennai, Tamil Nadu, India | [5]School of Sustainability, Indian Institute of Technology Madras (IIT Madras), Chennai, Tamil Nadu, India

Correspondence: Ravi Kumar (nvrk@iitm.ac.in)

Received: 30 June 2026 | **Revised:** 9 September 2026 | **Accepted:** 11 September 2026

Keywords: flash roasting | point defects | reactive flash sintering | ZnO | ZnS roasting

ABSTRACT

Flash roasting, an adaptation of reactive flash sintering, enables rapid synthesis of dense ZnO from ZnS through simultaneous roasting and densification in a single step. Phase-pure ZnO was obtained at a minimum current density of 40 mA/mm^2 within 60 s at a furnace temperature of 650 °C, albeit with less densification. A relative density of ~95% was achieved at 100 mA/mm^2 with an average grain size of ~0.4 μm. Detailed microstructural analyses revealed the formation of shell-like structures during flash roasting, attributed to power bursts during traditional flash roasting that resulted in inhomogeneities in densification and microstructure. These issues were minimized using current-controlled flash roasting, resulting in controlled grain growth and a narrow grain size distribution. Spectrochemical analysis confirmed the presence of oxygen vacancies, indicating their potential use in resistive switching applications. The introduction of these vacancies reduced the optical band gap of ZnO from 3.370 to 3.225 eV. A ZnO device using Pt electrodes was fabricated, and its memristive response was investigated under dark and illuminated conditions. The flash-roasted ZnO-based lateral memristive device exhibits pronounced hysteresis in its current–voltage response, demonstrating remarkable resistive switching behavior triggered by light (photon) interaction.

1 | Introduction

Reactive flash sintering (RFS) is a modification to the existing flash sintering technique, during which the stoichiometric mixture of precursor powders is directly converted into a single-phase and dense compound [1]. This technique has emerged as an energy-efficient one-step solution for material synthesis and densification. The applied electric field dramatically accelerates the reaction and sintering kinetics in this process. Taibi et al. [2] reported that the energy consumption during RFS of $BiFeO_3$-$BaTiO_3$ is 83% less than that of conventional methods. Gonzalez et al. [3] synthesized phase-pure $BiFeO_3$ from a powder mixture of Bi_2O_3 and Fe_2O_3 at a furnace temperature of 625 °C in a few seconds. Several ceramics, such as $MgAl_2O_4$, LLZO (Lithium Lanthanum Zirconate Oxide), LLTO (Lithium Lanthanum Titanate), α-Al_2TiO_5, $Gd_2Zr_2O_7$, high-alumina spinel, high-entropy ceramics, high-entropy oxides, and perovskites, have been synthesized by RFS [4].

ZnO-based devices have gained significant attention for their potential in neuromorphic computing due to their bipolar resistive switching, synaptic plasticity emulation, and optical responsiveness [5]. Further, ZnO-based devices, often structured with Indium Tin Oxide (ITO) as ITO/ZnO/ITO stacks or doped variants such as Mg-doped ZnO thin films, exhibit high on/off ratios, stable retention, and multilevel conductance states suitable for memory and logic applications [5, 6]. ZnO is potentially used in solar cells [7], sensors [8], luminescence devices [9], optoelectronic devices [10], and resistive switching devices [11], including photocatalysts

All rights reserved, including rights for text and data mining and training of artificial intelligence technologies or similar technologies.
© 2026 Wiley-VCH GmbH.

[12–15]. Defects such as oxygen vacancies and zinc interstitials enhance resistive switching in ZnO-based memristors by enabling conductive filament formation [6]. A resistive switching device shows a reversible change in resistance under applied voltage due to defect migration, enabling nonvolatile memory [16]. When the resistance varies gradually and depends on previous electrical stimuli, it is called a memristor. If light is additionally used to modulate conductivity through photo-generated carriers or defect modification, it functions as a photonic synapse [17, 18]. Recent studies highlight their ability to mimic short-term memory and paired-pulse facilitation under light stimulation, achieving very high accuracy through reservoir computing [6]. This has established them as promising candidates for energy-efficient visual neuromorphic systems.

Conventional ZnO synthesis methods, such as solvothermal, hydrothermal, and controlled precipitation, require multiple processing steps at elevated temperatures and take several hours to several days to produce fine ZnO powders [19]. Similarly, conventional metallurgical roasting requires temperatures of 600–1100 °C and several hours to convert ZnS into ZnO, followed by an additional high-energy sintering step to produce dense pellets. Recently, flash roasting, an adaptation of the RFS, has been an efficient method for the rapid production of ZnO from ZnS powder [20]. Similar to RFS, flash roasting involves simultaneously subjecting the green ZnS compact to an external electric field and an elevated furnace temperature. Due to the application of the electric field, the synthesis of ZnO occurs via a roasting reaction (conversion of ZnS to ZnO), as well as the densification of the roasted product, i.e., ZnO, in a few seconds only. As a result, roasting and densification occur together in a single step [20]. During electrification, ZnO synthesis through ZnS roasting and densification of the formed ZnO occur simultaneously in a single step. In another set of experiments, the flash-sintered ZnO showed relative densities between 93.6% and 97.1%, and conductivities between 205 and 590 S/cm [21]. This is attributed to the high concentrations of donor-type defects, such as oxygen vacancies and zinc interstitials. These point defects are introduced due to field-enhanced ionization during the process and eventually drive electrothermal runaway and accelerated densification far beyond equilibrium processing limits [21, 22]. The given conductivity range is higher than that of undoped ZnO ceramics prepared by different methods. Furthermore, different electrification strategies have been reported in the literature to enhance conduction in ZnO [23, 24].

Defect-engineered ZnO can be prepared by either flash sintering of ZnO or flash roasting of ZnS. In flash sintering, defects are mainly formed through electrothermal effects, which result from the combined action of an applied electric field and Joule heating. In contrast, RFS generates defects not only due to the electric field but also because of strong lattice disturbances caused by a phase transformation during the chemical reaction. Along with the a-thermal effects caused by the electric field, the breaking and reforming of atomic bonds to create a new crystal structure introduce additional structural defects [4, 25]. Therefore, flash roasting of ZnS could be a simple and effective method to produce a high concentration of point defects as compared to the flash sintering of ZnO.

In this study, we report the isothermal (IST) flash roasting of ZnS to produce ZnO pellets under voltage-controlled (traditional flash) and current-controlled (CC) modes. Spectrochemical characterization and band gap analysis were performed to investigate the oxygen vacancies introduced during processing and their influence on functional properties for memristor applications. Further, a ZnO device with platinum electrodes was fabricated, and its memristive response was evaluated to assess its potential for photonic synapse applications. Further, the light-sensitive oxygen vacancies generated during flash roasting strongly affect the memristive behavior of the material, which has also been reported.

2 | Experimental Procedure

Commercial ZnS powders (Aldrich Chemistry, 10 µm, 99.99% trace-metal basis) were milled in deionized water with 5 wt.% binder (Duramax B-1000) and dried in an oven at 80 °C. The dried powders were cold-pressed into dog-bone-shaped pellets having a gauge length of 15 mm, width of 3.5 mm, and thickness of ~1.5 mm. Binder burnout was not performed, as it may initiate the roasting of the ZnS samples before flash experiments. Platinum paste was applied in the vicinity of the holes in the ear section of the dog-bone samples for better electrical contact.

The sample was suspended in the center of the horizontal tubular furnace (Ants Innovation Pvt. Ltd., 3.5 kW) with a pair of platinum wires. An electric field was applied through a 600 W Sorensen DC power source (Sorensen DLM 300-2). A digital multimeter (Keithley 2000) was connected in series to monitor the current flow. A DC servo motor-driven linear slider with a lead screw mechanism enables precise, software-controlled sample positioning, ensuring optimal placement at the furnace center. The schematic of the setup that was used for flash roasting is shown in Figure 1. An Indian patent with patent application number 202641055272 has been filed for this custom-built setup of flash sintering/processing.

IST flash roasting experiments were done in both voltage control (VC) mode and current control (CC) mode at a furnace temperature of 650 °C under an applied electric field of 200 V/cm at various current densities (CD). The samples were held in stage III of the flash for different hold times before the power supply was turned off. Further, additional flash roasting was also performed at higher current density and longer holding time to understand their role in microstructural evolution. Higher CD flash roasting experiments were performed at CD of 120 and 240 mA/mm^2, keeping other parameters identical. To see the effect of longer holding time, flash roasting experiments were carried out at a CD of 100 mA/mm^2 with a holding time of 60 min, while keeping other parameters identical. A current-controlled (CC) flash roasting experiment was also

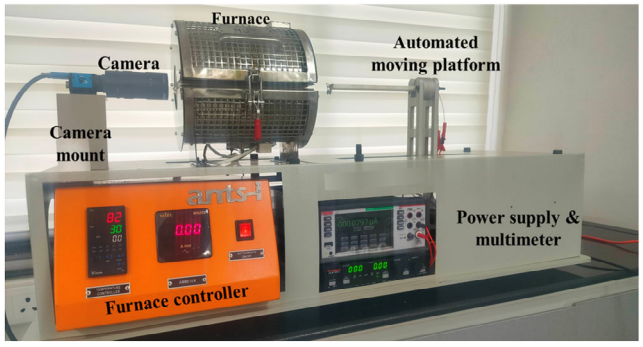


FIGURE 1 | Experimental setup used for flash roasting experimentation.

15272648, 0, Downloaded from https://advanced.onlinelibrary.wiley.com/doi/10.1002/adem.71296 by Central Library The Librarian, Wiley Online Library on [11/10/2026]. See the Terms and Conditions (https://onlinelibrary.wiley.com/terms-and-conditions) on Wiley Online Library for rules of use; OA articles are governed by the applicable Creative Commons License

performed to prevent power bursts and inhomogeneity in densification with controlled grain growth. An electric field of 200 V/cm was applied to the ZnS green compact at a furnace temperature of 650 °C, and the current was increased at a constant rate of 300 mA/min, with the target current density set at 100 mA/mm^2. The video of the experiment is attached in the Video S1. The total time taken to reach the target current density was 106 s.

VC mode was used for temperature measurement of the samples. The third stage of VC mode is considered the equilibrium stage where the current flowing through the sample becomes nearly constant, the voltage assumes stable values, and the power dissipation approaches a relatively stable value. Therefore, the temperature can be measured more reliably and interpreted more accurately [26, 27].

To estimate the sample temperature using the pyrometer, a new set of IST flash roasting experiments was conducted at a furnace temperature of 650 °C and three CD of 40, 80, and 120 mA/mm^2 in VC mode. The emissivity value was set to 0.9. The sample surface temperature in stage III was recorded through a laser infrared pyrometer with laser spot marking (Micro-epsilon CT Laser, CTLM-3H3SF300-C3). Three measurements were performed for each current density, and the average values were considered, with the laser spot initially positioned at the center of the 15 mm gauge section of the sample. Since shrinkage occurs during flash sintering, the laser spot position was continuously adjusted to maintain proper focus on the sample.

The ear sections of the roasted pellets were removed, and the gauge section was crushed into powder using an agate mortar and pestle. Phase analysis was carried out through X-ray diffraction (XRD) in a Panalytical diffractometer (PXRD, Empyrean, Malvern Panalytical, UK) using the Cu-Kα radiation ($\lambda = 0.1541$ nm) with a step size of 0.02° and a scan rate of 2°/min in a two-theta range of 20°–75°. Raman spectroscopy was performed using the Indiram Ctr Series, Technos Instruments, attached with a charge-coupled device (CCD) detector. A laser light ($\lambda = 532$ nm) was used as the excitation source, while the spectra were collected in the range of 100–800 cm^{-1} with an accumulation time of 30 s. To carry out the microstructural analyses, the samples were broken in the middle of the gauge section, and the fractured surface was observed in an FEG-SEM equipped with an energy-dispersive spectroscopy (EDS) detector (Elite Plus, EDAX). Before imaging, the samples were sputter-coated with a thin film of gold to prevent charging. Average grain size was measured through the linear intercept method. The initial ZnS powder was characterized using SEM. The results are shown in Figure S1. The ZnS powder shows a general flaky morphology.

Room-temperature electron paramagnetic resonance (EPR) spectroscopy and X-ray photoelectron spectroscopy (XPS) were performed for defect characterization. JEOL (JES 200) was used for EPR with a sensitivity of 7 x 10^9 spins/0.1 mT, while the operating frequency of X-band was ~9.4 GHz. The photoelectron spectra for Zn_{2p} and O_{1s} were collected using the Thermo Scientific K-Alpha. The Al-K_α line was used as a probe X-ray source, and peak fitting and data analysis of XPS were performed using XPSPEAK 41 software. To study the optical properties of the powder sample, the diffuse reflectance spectrum (DRS) of the sample was measured using a UV–vis spectrophotometer (SHIMADZU, UV-2600) with an integrating sphere attachment. To determine the optical band gap (Eg) of flash-roasted ZnO, the Kubelka–Munk approach has been adopted. A plot of $(F(R)h\nu)^2$ versus $h\nu$ is shown in Figure S2. The value of the optical bandgap was determined by extrapolating the linear portion of the plot to $((F(R)h\nu)^2 = 0)$ [28]. The same Kubelka–Munk approach was adopted to determine the band gap of the as-received ZnS sample for reference purposes.

We further investigated the memristive potential of the flash-roasted ZnO sample. The schematic of the fabricated lateral memristive device with the electrical response measurement setup is presented in Figure 2. Platinum (Pt) metal pads of 1 × 1 mm were deposited using the e-beam evaporation technique (HHV AUTO 500) with a 100 μm gap on the flash-roasted ZnO and as-received ZnS (for comparison) to make lateral resistive switching devices or memristors. To examine the effect of light (365 nm) on the flash-roasted ZnO and as-received ZnS material-based lateral memristive device, voltage was applied in a range of −1.5 to 1.5 volts on one metal pad by keeping the other metal pad grounded, and its current–voltage response was observed using a Keithley 2450 source meter. To study the resistive switching or memristive behavior of the fabricated lateral memristive devices using as-received ZnS and ZnO samples as resistive switching material, a voltage sweep was applied in the sequence 0 V → 1.5 V → 0 V → −1.5 V → 0 V with a step size of 0.1 V/s by keeping the compliance current 1 mA at room temperature, while grounding one metal electrode.

3 | Results

3.1 | Voltage-Controlled (VC) Flash Roasting

At a current density of 20 mA/mm^2, the current followed a preferred conduction path, resulting in localized roasting and densification only along that path. The remaining regions of the sample were largely unaffected. As a result, the sample showed

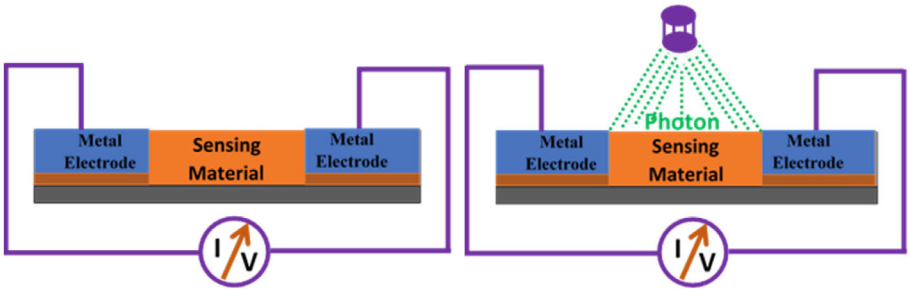


FIGURE 2 | Schematic of the fabricated lateral memristive device and electrical measurement setup.

15272648, 0, Downloaded from https://advanced.onlinelibrary.wiley.com/doi/10.1002/adem.71296 by Central Library The Librarian, Wiley Online Library on [11/10/2026]. See the Terms and Conditions (https://onlinelibrary.wiley.com/terms-and-conditions) on Wiley Online Library for rules of use; OA articles are governed by the applicable Creative Commons License

no significant shrinkage. This behavior can be seen in Video S2. Similar preferential current flow behavior has already been reported in the literature [29]. Figure 3a–c show the electric field, current density, and power density profiles of 40, 60, 80, and 100 mA/mm^2, in different experiments, respectively. The samples flashed immediately at the set furnace temperature of 650 °C. The current profiles remained smooth throughout the experiment without any noticeable fluctuations.

The results of the XRD analysis are shown in Figure 4a. The initial ZnS powder mainly exhibited a cubic zinc blende crystal structure. After flash roasting at 40 mA/mm^2, the X-ray diffractogram showed the peaks of ZnO (JCPDS 00-036-1451), indicating successful phase transformation. The diffractograms of the flash-roasted sample at higher CD of 60, 80, and 100 mA/mm^2 have been shown in Figure S3. Localized structural analysis using Raman spectroscopy (Figure 4b) also confirmed the formation of the ZnO phase at a current density of 40 mA/mm^2. These results demonstrate that complete roasting (oxidation) of ZnS was achieved at this current density and within 60 s at a furnace temperature of 650 °C. It was further confirmed by the EDS results, as no sulfur signal was detected from the flash-roasted sample, i.e., Figure S4.

The flash roasting was carried out for 60 s, as the main aim was to obtain dense ZnO samples. It has been reported in previous work that within 10 s, the conversion of ZnS to ZnO happens [20]. So, in our case also, the complete conversion of ZnS to ZnO happened in 10 s, whereas densification continued during the remaining 50 s of the experiment. Therefore, during flash roasting at 40 mA/mm^2 and a furnace temperature of 650 °C, a holding time of 60 s was sufficient to obtain phase-pure ZnO. However, the densification was limited, and the relative density achieved was only about 78% (Table 1). As the current density

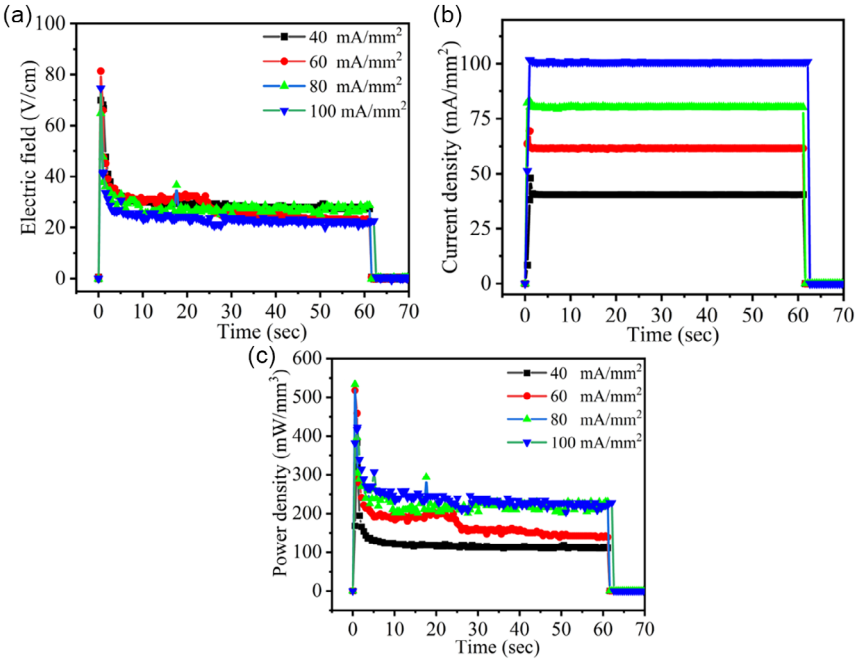


FIGURE 3 | Characteristic plot of flash roasting experiment performed at 650 °C under an applied electric field of 200 V/cm for: (a) electric field versus time, (b) current density versus time, and (c) power density versus time.

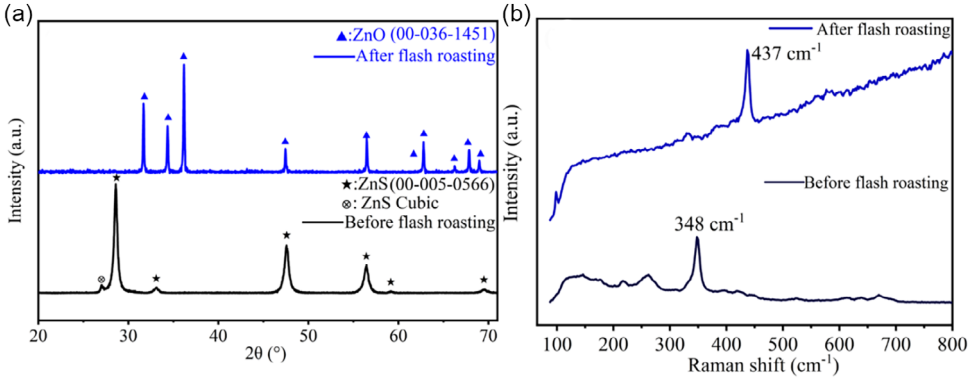


FIGURE 4 | (a) XRD and (b) Raman spectra of samples before (as-received ZnS powder) and after flash roasting performed at a furnace temperature of 650 °C and a current density of 40 mA/mm^2.

15272648, 0, Downloaded from https://advanced.onlinelibrary.wiley.com/doi/10.1002/adem.71296 by Central Library The Librarian, Wiley Online Library on [11/10/2026]. See the Terms and Conditions (https://onlinelibrary.wiley.com/terms-and-conditions) on Wiley Online Library for rules of use; OA articles are governed by the applicable Creative Commons License

TABLE 1 | | List of flash roasting (FR) parameters (electric field and current density), mean grain size, and relative density of flash-roasted samples.

Current density, mA/mm^2	Electric field, V/cm	Holding time, min	Mean grain size, nm	Relative density, %	Remarks
40	200	01	250 ± 95	78	Traditional (IST) FR
60	200	01	270 ± 100	85	
80	200	01	280 ± 90	92	
100	200	01	406 ± 100	95	
100	200	60	1198 ± 201	98	
100	—	—	776 ± 152	96	Current-controlled FR (300 mA/min)

increased from 40 to 100 mA/mm^2, an increase in grain size and relative density was observed. The results are compiled in Table 1. This behavior is mainly attributed to the higher sample temperature generated at higher CD due to increased Joule heating. The enhanced thermal energy promotes faster mass transport and grain growth, leading to improved densification. In addition, higher current density accelerates the oxidation and sintering processes, resulting in a more compact microstructure with reduced porosity [25].

The relative density of ~95 % was observed for the flash-roasted sample at the current density of 100 mA/mm^2. However, the observed microstructure revealed unusual, clustered features in the flash-roasted sample regions (marked by arrows) of Figure 5a–c. Dense shell-like clusters with internal pore structures were observed at several locations in the microstructure, in the marked regions. In these regions, multiple grains were sintered together to form hollow shell-like structures. Similar shell-like features were still observed at higher CD of 120 and 240 mA/mm^2, as can be seen from Figure S5. These structures may form due to the simultaneous roasting and densification process, where the SO_2 gas produced during oxidation becomes temporarily trapped inside the densifying shell. This can create internal pores and hollow regions within the clusters. However, it is to be noted that, after holding the sample in the flash state for 60 min at a CD of 100 mA/mm^2, the shell-like structures disappeared, as shown in Figure 5d,e. The longer holding time also resulted in significant grain growth, with the average grain size increasing to about 1200 nm.

3.2 | Current-Controlled (CC) Flash Roasting

The images of the sample before and after flash roasting are shown in Figure 6a,b, respectively.

The electrical characteristics and microstructural results of the current-controlled flash roasting are shown in Figure 7(a-b) and 7(c-d), respectively. The microstructure under CC shows no shell structure, with a uniform grain size and a narrow grain size distribution with minimal grain growth. The gradual current injection during current-controlled flash roasting resulted in uniformly distributed grains, in contrast to the agglomerated structure that was observed during VC flash roasting (i.e., Figure 5a–c). Since the current-controlled flash roasting process produced a uniform microstructure and achieved a relative density of 96% (Table 1),

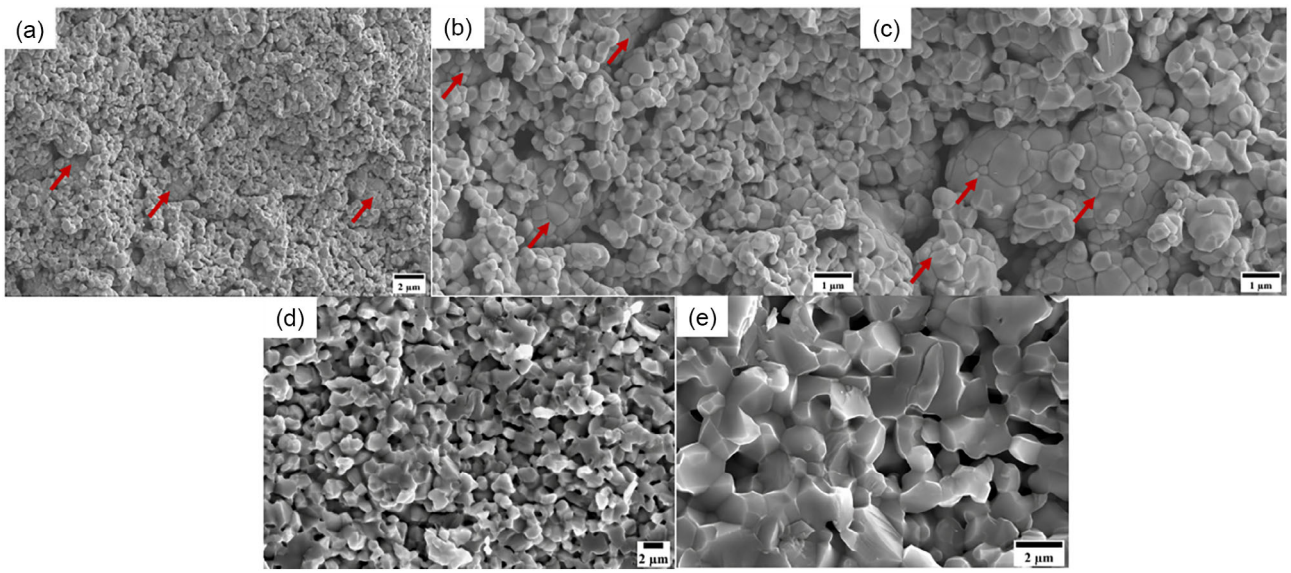


FIGURE 5 | High-resolution SEM micrographs of a flash-roasted ZnO sample processed at a furnace temperature of 650 °C and at 100 mA/mm^2. Here, (a–c) correspond to a hold time of 60 s, while (d,e) correspond to a hold time of 60 min.

15272648, 0, Downloaded from https://advanced.onlinelibrary.wiley.com/doi/10.1002/adem.71296 by Central Library The Librarian, Wiley Online Library on [11/10/2026]. See the Terms and Conditions (https://onlinelibrary.wiley.com/terms-and-conditions) on Wiley Online Library for rules of use; OA articles are governed by the applicable Creative Commons License

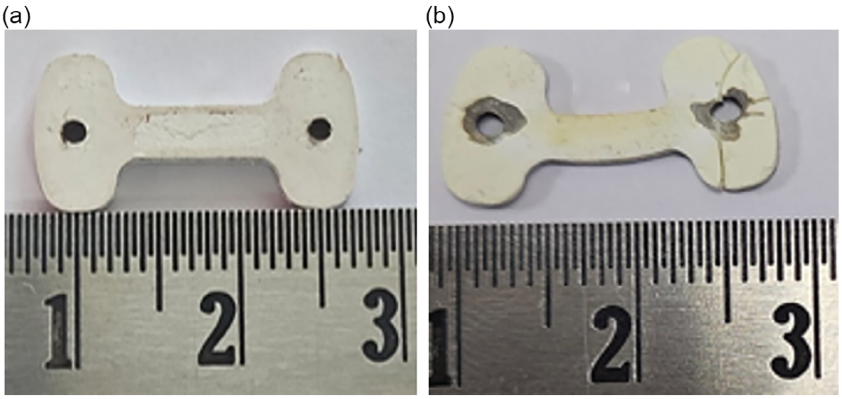


FIGURE 6 | Images of the sample before and after flash roasting.

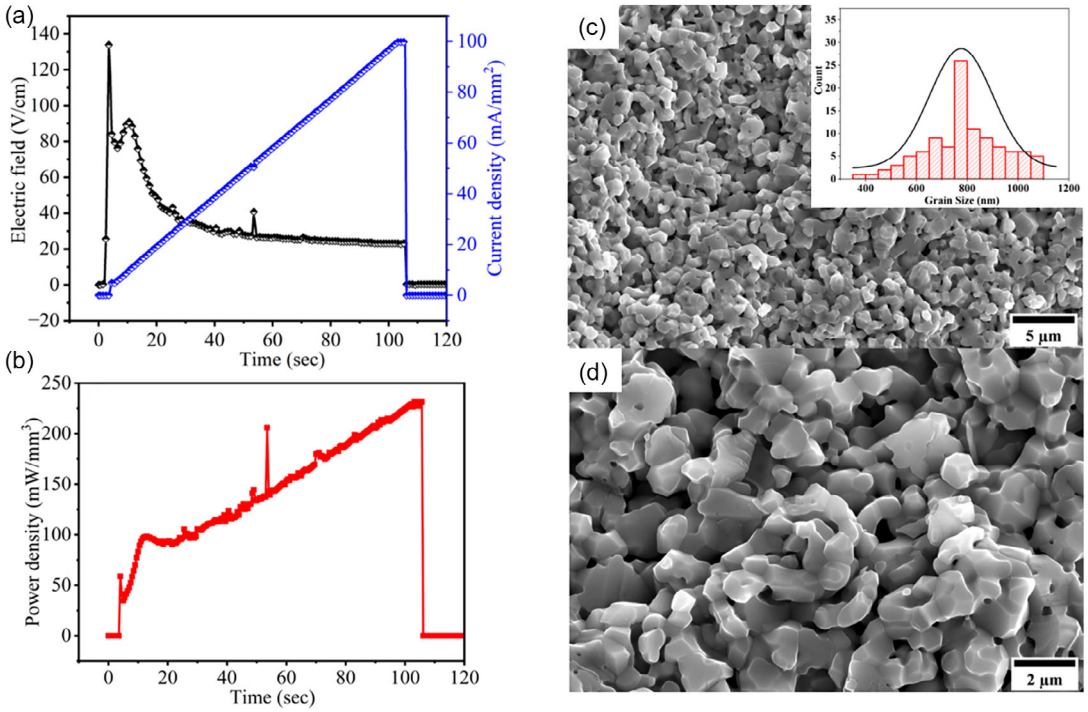


FIGURE 7 | Plot of (a) electric field and current density with respect to time; (b) power density with respect to time; and (c,d) correspond to high-resolution SEM micrographs for the current-controlled flash roasting at 650 °C with a current ramp rate of 300 mA/min and a target current density of 100 mA/mm^2.

this sample was selected as the optimized specimen for evaluating its properties and its potential memristive performance.

The bandgap of the flash-roasted ZnO sample was found to be 3.225 eV (Figure 8a), which is slightly lower than the literature-reported value of 3.370 eV for bulk ZnO [28, 30]. The bandgap of the as-received ZnS powder was found to be 3.606 eV, as can be seen from Figure S2. Figure 8b shows the EPR spectra of flash-roasted ZnO. Zn^{2+} is EPR silent as it has no paramagnetic center due to the absence of an unpaired electron. The $g \sim 2.007$ corresponds to an electron trapped by oxygen vacancies ($V_{\dot{O}}$), which further suggests that the flash-roasted ZnO is deficient in oxygen. The $g \sim 2.010$ indicates the presence of adsorbed oxygen in the materials. In the literature, the reported values of "g" for oxygen vacancy and adsorbed oxygen are 2.003 and 2.068 [31]. The change in "g" value in this case can be attributed to increased concentration of localized density of electrons on neighboring atoms [32–34].

The XPS spectra of the flash-roasted sample are shown in Figure 8c,d. The XPS plot was calibrated with respect to $C1_s$ and is shown in Figure S6. The high-resolution O_{1S} and Zn_{2p} were fitted using the linear background and Gaussian function to obtain reduced chi-square (χ^2), which is attached in the Table S1. XPS spectra of O_{1s} were fitted into two Gaussian peaks. The peaks at binding energies of 529.8 and 531.7 eV are assigned to lattice oxygen and oxygen vacancy, respectively. The binding energies of 1021.9 and 1045 eV correspond to $Zn2p_{3/2}$ and $Zn2p_{1/2}$, respectively. Similar binding energies for O_{1s} and Zn_{2p} have been well reported in the literature [35, 36].

15272648, 0, Downloaded from https://advanced.onlinelibrary.wiley.com/doi/10.1002/adem.71296 by Central Library The Librarian, Wiley Online Library on [11/10/2026]. See the Terms and Conditions (https://onlinelibrary.wiley.com/terms-and-conditions) on Wiley Online Library for rules of use; OA articles are governed by the applicable Creative Commons License

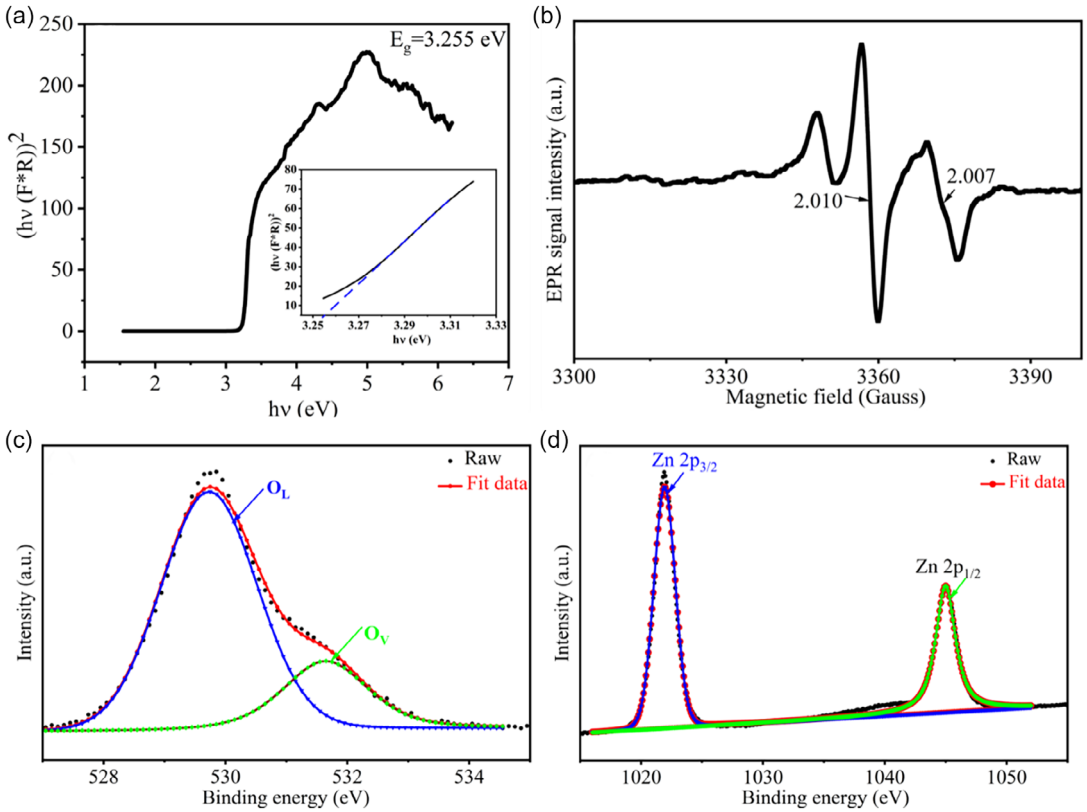


FIGURE 8 | Plot of (a) optical band gap; (b) first harmonic EPR spectra; (c) XPS spectra of O_{1s}; and (d) XPS spectra of Zn_{2p} for the ZnO sample derived from flash roasting of ZnS.

3.3 | Measurement of Sample Temperature

The pyrometer readings at a furnace temperature of 650 °C with CD of 40, 80, and 120 mA/mm^2 were 680, 730, and 780 °C, respectively (Figure 9), with a standard deviation of 15 °C. It should also be noted that sample temperature measurement using a laser pyrometer is based on the radiation emitted by the specimen and also on the emissivity of the material. During electrically assisted flash roasting, power can be consumed not only in radiation but also in defect generation, considering the nonequilibrium nature of the process [37]. Furthermore, the luminescence coming from the sample interferes with the laser of the pyrometer.

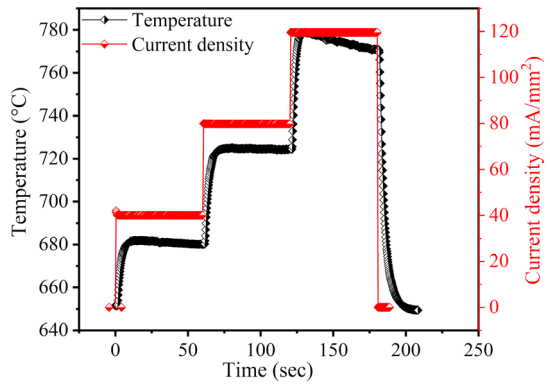


FIGURE 9 | Plot of sample temperature measured using a laser pyrometer at current densities of 40, 80, and 120 mA/mm^2.

On a technical note, the roasting temperature of zinc sulfide to zinc oxide can be reduced in the presence of lattice defects and/or vacancies. Defect sites such as zinc or sulfur vacancies created during the flash process can act as potential sites for initiation of oxidation reactions. Also, one may expect reduced activation energy required to start the oxidation reaction due to an exothermic reaction on a defective surface, resulting in the formation of metal–oxygen bonds at relatively lower temperatures. Therefore, we believe the specimen temperature during flash roasting of ZnS to ZnO will be much lower than the conventional roasting temperature.

The current–voltage response, as shown in Figure 10a,b, signifies that the flash-roasted ZnO sample is photon-sensitive. The current–voltage response of the initial ZnS sample was also included to avoid confusion regarding the pre-existing defect density, which is shown in Figure 10c. It indicates that the ZnS-based lateral memristive device exhibits negligible hysteresis in its current–voltage response under both dark and light conditions, indicating a very small amount of resistive switching or memristive behavior. In contrast, Figure 10d shows that the flash-roasted ZnO-based lateral memristive device exhibits pronounced hysteresis in its current–voltage response under dark and light exposure, demonstrating remarkable resistive switching behavior triggered by light (photon) interaction. These findings suggest ZnO sample derived from flash-roasting of ZnS can possibly be an alternative material for photonic synapse applications.

15272648, 0, Downloaded from https://advanced.onlinelibrary.wiley.com/doi/10.1002/adem.71296 by Central Library The Librarian, Wiley Online Library on [11/10/2026]. See the Terms and Conditions (https://onlinelibrary.wiley.com/terms-and-conditions) on Wiley Online Library for rules of use; OA articles are governed by the applicable Creative Commons License

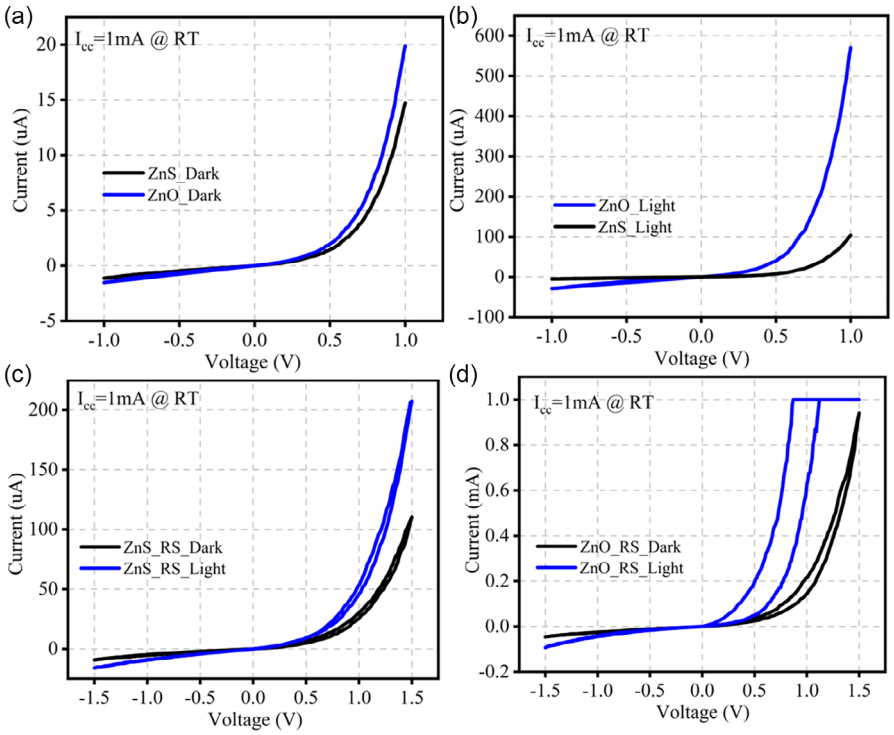


FIGURE 10 | I–V characteristics of the ZnO sample derived from flash roasting of ZnS under (a) dark and (b) light, and memristive I–V of (c) ZnS and (d) flash-roasted ZnO devices in dark and light.

4 | Discussion

4.1 | Efficient ZnO Pellet Synthesis

The chemical reaction for the conversion of sulfides into oxides is shown below in Equation (1).

$$2ZnS + 3O_2 \rightarrow 2ZnO + 2SO_2 \quad (1)$$

The flash roasting method enables complete roasting and densification in a single step within 60 s at a furnace temperature of 650 °C, producing dense, phase-pure ZnO. The use of an electric field, along with thermal treatment, has enhanced this reaction by several orders of magnitude at a much lower temperature [20]. In contrast, during conventional roasting, the reaction typically occurs in a temperature range of 600–1100 °C and is sluggish, as the process depends on several parameters such as gas flow rate, concentrate mass, processing time, and temperature, and requires complex machinery [38]. Moreover, it produces ZnO powder, and densification is performed as a separate step at 900–1200 °C for 60–120 min [39]. However, flash roasting enables very rapid processing at much lower furnace temperatures (around 650 °C), typically 500–600 °C lower than those used in conventional sintering (1100–1200 °C) [20, 38]. High densities above 95% can be achieved within a few seconds (Table 1).

4.2 | Microstructural Evolution

SO_2 gas is released as a byproduct of the flash roasting of ZnS, as shown in Equation (1) . Cannon et al. [40] have explained in their studies about the gas–solid reaction during the oxidation of ZnS. The initial ZnS powder particles have an agglomerated flaky structure, as can be seen from Figure S1. Conventionally, the roasting reaction starts from the surface of particles or agglomerates. During oxidation, the ZnS core was gradually covered by a layer of ZnO that sticks to the surface. This oxide layer acts as a barrier to the reaction. For the reaction to continue, oxygen must diffuse inward through the ZnO layer, while SO_2 gas must diffuse outward. According to this study [40], at temperatures below about 880 °C, this gas movement is fast, so the reaction rate is mainly controlled by the chemical reaction at the ZnS–ZnO interface. However, above 880 °C, diffusion through the oxide layer becomes slower and starts to control the overall reaction rate. Above about 950 °C, the oxide layer becomes dense and almost impermeable, strongly restricting oxygen flow. This leads to a buildup of internal gas pressure from ZnS decomposition, which can lift the oxide layer and form blisters or eruptions. In addition, since the oxidation reaction is exothermic, heat can become trapped beneath the oxide layer at temperatures above 900 °C. This causes a local temperature increase, which accelerates the reaction unevenly and results in non-uniform oxide growth [40, 41]. This effect could be more pronounced when heating is fast, or densification occurs early, as in the case of flash roasting, because these conditions prevent smooth gas escape and promote pore formation instead of uniform densification. The aforementioned reason is likely to contribute to the distinct observed microstructure, as shown in Figure 5a–c during the flash roasting of ZnS.

An argument may arise based on the data presented from IST experiments conducted under similar conditions in previous studies, suggesting that the roasting reaction is largely completed before significant pore closure begins during densification [20]. It has been reported that the roasting process is completed within the first 10 s, whereas densification continues during the remaining 50 s [20]. This argument is further supported by the fact that

15272648, 0, Downloaded from https://advanced.onlinelibrary.wiley.com/doi/10.1002/adem.71296 by Central Library The Librarian, Wiley Online Library on [11/10/2026]. See the Terms and Conditions (https://onlinelibrary.wiley.com/terms-and-conditions) on Wiley Online Library for rules of use; OA articles are governed by the applicable Creative Commons License

sintering is generally controlled by slower-diffusing species, while phase transformation is governed by relatively faster-moving species; therefore, phase transformation typically precedes densification during the process [42]. In the present case, the results also agree with the argument, as the relative density data compiled in Table 1 show that these hollow shell structures have not much effect on the densification. Since IST flash processing suffers from nonuniform densification and several hotspot formations, the non-uniform roasting could be the reason for the shell-like structure formation at several places. These structures are formed due to the very high kinetics of the traditional flash roasting process; however, the roasting reaction is largely completed at the start of the flash. Furthermore, VC flash processing is accompanied by the sudden shrinkage (shown in Video S3), suggesting that the majority of densification happens during the start of the flash itself. The competition between the densification and roasting processes after the start of the flash may also result in the entrapment of the gases, and that could eventually result in these shell-like structures.

Rapid roasting and densification during the process can lead to the formation of mechanically unstable shell structures. These shells cannot maintain their integrity during the gas–solid reaction. As explained earlier, the shell forms because gases generated inside cannot escape easily, which leads to a buildup of internal pressure. As a result, high thermal stresses may develop within the shell. A short holding time (e.g., 60 s, Figure 5a–c) is not sufficient to relieve these stresses. Increasing the holding time allows the internal pressure and thermal stresses to relax, which can cause the shell structures to collapse. This behavior is shown in Figure 5d,e, where the structures disappear when the holding time is increased up to 60 min. However, longer holding times also lead to undesirable grain growth (Table 1).

The current-controlled (CC) flash roasting process overcomes the problems mentioned above because it avoids power bursts and hotspot formation [43]. In contrast, traditional flash sintering often experiences power surges during the second stage of flash, which leads to a nonuniform microstructure [44]. Similarly, IST flash roasting can also result in nonuniform densification. In the current-controlled method, the gradual application of current prevents sudden power spikes at the onset of the flash, thereby avoiding overheating and possible damage [43, 45]. As a result, roasting and densification occur more uniformly, producing a narrow grain size distribution and controlled grain growth, as shown in Figure 5. This approach also provides better control over power input and temperature distribution, making it suitable for temperature-sensitive materials [20]. Consequently, more uniform microstructures are obtained, as observed in the present case (Figure 7).

4.3 | Point Defect Generation

Reactive flash processing generates vacancies, much above the equilibrium limits, in ceramics by applying strong electric fields in combination with temperatures, which accelerates the reaction and concurrent densification well beyond conventional limits [1, 4]. These defects get ionized by the electric field through the Frenkel defect mechanism, producing neutral defects and electron–hole pairs. The neutral defects assist densification by moving vacancies toward grain boundaries and interstitials toward pores, while recombination of electron–hole pairs causes luminescence [22, 46]. The extreme Joule heating with very high heating rates and cooling rates could suppress the annihilation and segregation of defects that occur with gradual heating. This results in supersaturated defect concentrations that endure because of the rapid quench rates after the flash. XPS and EPR results show the oxygen vacancy concentration beyond equilibrium limits. Furthermore, retention of point defects is thought to contribute to lowering the band gap of ZnO by splitting the energy levels [47]. Soriano et al. [48] reported that the presence of point defects, such as vacancies, can lower the band gap by changing the strength and symmetry of the crystal field. This is evident from Figure 8a.

Reactive flash processing induces exceptionally high diffusion rates. Studies on oxide electrification report diffusion coefficients of ~10^{-10} m^2 s^{-1}, approximately six orders of magnitude higher than conventional tracer diffusion values [22]. Likewise, the hexagonal ZnS phase emerges during the electrification of ZnS roasting at temperatures well below its equilibrium phase transformation temperature. Moreover, this high-temperature hexagonal phase was retained even after cooling to room temperature [20]. In the present case, the maximum temperature of the sample was found to be 780 °C at a current density of 120 mA/mm^2, as measured using a laser pyrometer (Figure 9). In contrast, this phase conventionally appears above 1020 °C only in the Zn–S phase diagram [49]. The stabilization of this phase at nonequilibrium temperature is attributed to the defects generated during the flash processing [20, 50]. Furthermore, flash sintering is well known to generate point defects, mostly anionic vacancies in the oxide ceramics [45, 51]. There are reports of the formation of metastable phases in the state of flash [52]. However, most of the metastable phases are transient and disappear when the electric field is turned off. The formation of these phases is also attributed to the generation of point defects in the state of flash [50]. Furthermore, the introduction of dopants can also promote vacancy formation in ZnO by altering the lattice structure. Such defect generation mechanisms in ZnO have been widely reported in the literature [53, 54]. In the conventional route, the formation of defects takes place sluggishly through thermal treatment; on the contrary, the flash process generates defects rapidly due to the applied electric field and rapid heating. Flash roasting, therefore, could be a new pathway to produce defect-engineered ZnO in a very rapid and efficient manner.

4.4 | Memristive Behavior

The underlying physics for resistive switching in ZnO-based memristive devices is the migration of oxygen vacancies and/or the change in their concentration [5, 22, 55]. These defects can be controlled by doping, heat treatment, substrate temperature, and photon excitation. Under external stimuli such as light, electric field, or UV exposure, some frozen defects can become mobile. This changes the conductivity or resistance of the material [35, 55]. ZnO-based lateral memristors show stronger resistive switching under light conditions compared to dark conditions. This behavior is due to light-sensitive oxygen vacancies. When UV or visible-light is applied, electron–hole pairs are generated. The holes are trapped by neutral oxygen vacancies, which become ionized [56]. This increases the free electron concentration and reduces the Schottky barrier width, resulting in higher

15272648, 0, Downloaded from https://advanced.onlinelibrary.wiley.com/doi/10.1002/adem.71296 by Central Library The Librarian, Wiley Online Library on [11/10/2026]. See the Terms and Conditions (https://onlinelibrary.wiley.com/terms-and-conditions) on Wiley Online Library for rules of use; OA articles are governed by the applicable Creative Commons License

conductance. From Figure 10d, the ZnO-based lateral memristor clearly demonstrated enhanced resistive switching under light with a wavelength of 365 nm.

The defect-engineered ZnO produced via the optimized flash-roasting process provides a promising platform for tailoring charge transport, thereby enabling the investigation of photonic synapse behavior for neuromorphic computing applications. Furthermore, systematic optimization of both lateral and metal-insulator-metal (sandwich) device architectures will be undertaken using the optimized flash-roasting parameters.

5 | Conclusions

This study systematically investigated the flash roasting behavior of ZnS using both traditional isothermal flash roasting (IST) and current-controlled (CC) modes. Both processing routes were carried out at a relatively low furnace temperature of 650 °C, and the functional potential of the processed materials for photonic synapse applications was explored. Flash roasting of sulfides is a rapid and efficient route for producing ZnO with a high concentration of defects. In this process, ZnS is converted into defect-engineered ZnO pellets through simultaneous roasting and densification in a single step. The following conclusions can be drawn from the present work:

1. Traditional flash processing performed at 650 °C, 200 V/cm, and a current density of 100 mA/mm^2 produced dense pellets within 60 s of holding time. However, shell-like clusters were observed due to the inherent power bursts associated with the process occurring over a very short duration.
2. Flash roasting performed in current-controlled mode at the same furnace temperature resolved the microstructural inconsistencies observed in traditional processing. Phase-pure ZnO with a relative density of 98% was obtained in less than 2 min. The processed samples exhibited fine grains with a narrow grain size distribution.
3. The optical band gap of the ZnO sample derived from flash-roasting of ZnS was found to be lower (3.225 eV) than the conventionally reported value of ZnO (3.37 eV). This is attributed to the generation of defects during the processing.
4. XPS and EPR confirm the presence of oxygen vacancies in the ZnO sample derived from flash-roasting of ZnS.
5. The maximum temperature of the sample was found to be 780 °C, measured using a laser pyrometer at the current density of 120 mA/mm^2.
6. Oxygen vacancies play an important role in memristor devices because they facilitate resistive switching by enabling charge transport. The ZnO sample derived from flash-roasted ZnS shows improved resistive switching under light illumination, which is attributed to these defect states.

Acknowledgments

The authors would like to thank Rishi and Jyotsna Raj Center for Electrification of Materials Manufacturing (CR23242422MMDONO008275) for the financial support. The authors gratefully acknowledge the Flash Sintering Laboratory, IIT Patna, for providing valuable support for this work. The support obtained from SAIF at IIT Madras, India, under the Department of Science and Technology (DST), India, is greatly appreciated.

Funding

This work was supported by the Rishi and Jyotsna Raj Center for Electrification of Materials Manufacturing (Grant No. CR23242422MMDONO008275).

Conflicts of Interest

The authors declare no conflicts of interest.

Data Availability Statement

The data that support the findings of this study are available from the corresponding author upon reasonable request.

References

1. V. Avila, B. Yoon, R. R. I. Neto, et al., "Reactive Flash Sintering of the Complex Oxide $Li_{0.5}La_{0.5}TiO_3$ Starting From an Amorphous Precursor Powder," *Scripta Materialia* 176 (2020): 78–82, https://doi.org/10.1016/j.scriptamat.2019.09.037.

2. A. Taibi, S. Chaguetmi, P. E. Sánchez-Jiménez, et al., "Pure Perovskite $BiFeO_3$–$BaTiO_3$ Ceramics Prepared by Reaction Flash Sintering of $Bi2O_3$–Fe_2O_3–$BaTiO_3$ Mixed Powders," *Ceramics International* 47 (2021): 26947–26954, https://doi.org/10.1016/j.ceramint.2021.06.108.

3. E. Gil-González, A. Perejón, P. E. Sánchez-Jiménez, M. J. Sayagués, R. Raj, and L. A. Pérez-Maqueda, "Phase-Pure $BiFeO_3$ Produced by Reaction Flash-Sintering of $Bi2O_3$ and Fe_2O_3," *Journal of Materials Chemistry A* 6 (2018): 5356–5366, https://doi.org/10.1039/C7TA09239C.

4. B. Yoon, V. Avila, I. R. Lavagnini, J. V. Campos, and L. M. Jesus, "Reactive Flash Sintering of Ceramics: A Review," *Advanced Engineering Materials* 25 (2023): 2200731, https://doi.org/10.1002/adem.202200731.

5. R. Schmitt, J. Spring, R. Korobko, and J. L. M. Rupp, "Design of Oxygen Vacancy Configuration for Memristive Systems," *ACS Nano* 11 (2017): 8881–8891, https://doi.org/10.1021/acsnano.7b03116.

6. H. Jang, S. Kim, S. Ju, S. Park, S. Kim, and M.-H. Kim, "Multifunctional ZnO-Based Optical Memristors for Synapse–Neuron Integration and Neuromorphic Vision Systems," *Nanoscale* 17 (2025): 24566–24577, https://doi.org/10.1039/D5NR02736E.

7. W.-T. Jiang, C.-T. Wu, Y.-H. Sung, and J.-J. Wu, "Room-Temperature Fast Construction of Outperformed ZnO Nanoarchitectures on Nanowire-Array Templates for Dye-Sensitized Solar Cells," *ACS Applied Materials & Interfaces* 5 (2013): 911–917, https://doi.org/10.1021/am302570r.

8. W. Guo, T. Liu, L. Huang, H. Zhang, Q. Zhou, and W. Zeng, "HMT Assisted Hydrothermal Synthesis of Various ZnO Nanostructures: Structure, Growth and Gas Sensor Properties," *Physica E: Low-Dimensional Systems and Nanostructures* 44 (2011): 680–685, https://doi.org/10.1016/j.physe.2011.11.008.

9. J. Chen, Z. Feng, P. Ying, and C. Li, "ZnO Clusters Encapsulated Inside Micropores of Zeolites Studied by UV Raman and Laser-Induced Luminescence Spectroscopies," *Journal of Physical Chemistry B* 108 (2004): 12669–12676, https://doi.org/10.1021/jp048746x.

10. J. M. Lee, Y. B. Pyun, J. Yi, J. W. Choung, and W. I. Park, "ZnO Nanorod–Graphene Hybrid Architectures for Multifunctional Conductors," *Journal of Physical Chemistry C* 113 (2009): 19134–19138, https://doi.org/10.1021/jp9078713.

11. F. M. Simanjuntak, D. Panda, K.-H. Wei, and T.-Y. Tseng, "Status and Prospects of ZnO-Based Resistive Switching Memory Devices," *Nanoscale Research Letters* 11 (2016): 368, https://doi.org/10.1186/s11671-016-1570-y.

15272648, 0, Downloaded from https://advanced.onlinelibrary.wiley.com/doi/10.1002/adem.71296 by Central Library The Librarian, Wiley Online Library on [11/10/2026]. See the Terms and Conditions (https://onlinelibrary.wiley.com/terms-and-conditions) on Wiley Online Library for rules of use; OA articles are governed by the applicable Creative Commons License

12. B. Ludi and M. Niederberger, "Zinc Oxide Nanoparticles: Chemical Mechanisms and Classical and Non-Classical Crystallization," *Dalton Transactions* (2013): 12554–12568, https://doi.org/10.1039/C3DT50610J.

13. Y. Wang, X. Li, G. Lu, X. Quan, and G. Chen, "Highly Oriented 1-D ZnO Nanorod Arrays on Zinc Foil: Direct Growth From Substrate, Optical Properties and Photocatalytic Activities," *Journal of Physical Chemistry C* 112 (2008): 7332–7336, https://doi.org/10.1021/jp7113175.

14. M. Ahmad, Z. Hong, E. Ahmed, N. R. Khalid, A. Elhissi, and W. Ahmad, "Effect of Fuel to Oxidant Molar Ratio on the Photocatalytic Activity of ZnO Nanopowders," *Ceramics International* 39 (2013): 3007–3015, https://doi.org/10.1016/j.ceramint.2012.09.079.

15. J. Becker, K. R. Raghupathi, J. St. Pierre, D. Zhao, and R. T. Koodali, "Tuning of the Crystallite and Particle Sizes of ZnO Nanocrystalline Materials in Solvothermal Synthesis and Their Photocatalytic Activity for Dye Degradation," *Journal of Physical Chemistry C* 115 (2011): 13844–13850, https://doi.org/10.1021/jp2038653.

16. Y. Wang, Z. Lv, J. Chen, et al., "Photonic Flash Memory: Photonic Synapses Based on Inorganic Perovskite Quantum Dots for Neuromorphic Computing (Adv. Mater. 38/2018)," *Advanced Materials* 30 (2018): 1870287, https://doi.org/10.1002/adma.201870287.

17. R. Waser and M. Aono, "Nanoionics-Based Resistive Switching Memories," *Nature Materials* 6 (2007): 833–840, https://doi.org/10.1038/nmat2023.

18. J. J. Yang, D. Strukov, and D. Stewart, "Memristive Devices for Computing," *Nature Nanotechnology* 8 (2013): 13–24, https://doi.org/10.1038/nnano.2012.240.

19. A. A. Ismail, A. El-Midany, E. A. Abdel-Aal, and H. El-Shall, "Application of Statistical Design to Optimize the Preparation of ZnO Nanoparticles via Hydrothermal Technique," *Materials Letters* 59 (2005): 1924–1928, https://doi.org/10.1016/j.matlet.2005.02.027.

20. P. Rai and D. Yadav, "Flash-Induced Chemical Reaction: Conversion of a Sulphide Into Oxide and Its Densification in <10 s," *Materials Letters* 380 (2025): 137747, https://doi.org/10.1016/j.matlet.2024.137747.

21. Y. Liang, S. Xiang, and X. Zhang, "Fabrication of Highly Conducting Undoped ZnO Ceramics by Flash Sintering," *Journal of the European Ceramic Society* 44 (2024): 5989–5999, https://doi.org/10.1016/j.jeurceramsoc.2024.03.034.

22. S. I. A. Jalali and R. Raj, "Reactive Flash Sintering in a Bilayer of Zirconia and Lanthana: Measurement of the Diffusion Coefficient in Real Time," *Journal of the American Ceramic Society* 106 (2023): 867–877, https://doi.org/10.1111/jace.18804.

23. K. H. Kim, S. H. Shim, K. B. Shim, K. Niihara, and J. Hojo, "Microstructural and Thermoelectric Characteristics of Zinc Oxide-Based Thermoelectric Materials Fabricated Using a Spark Plasma Sintering Process," *Journal of the American Ceramic Society* 88 (2005): 628–632, https://doi.org/10.1111/j.1551-2916.2005.00131.x.

24. M. Søndergaard, E. D. Bøjesen, K. A. Borup, S. Christensen, M. Christensen, and B. B. Iversen, "Sintering and Annealing Effects on ZnO Microstructure and Thermoelectric Properties," *Acta Materialia* 61 (2013): 3314–3323, https://doi.org/10.1016/j.actamat.2013.02.021.

25. M. Biesuz and V. M. Sglavo, "Flash Sintering of Ceramics," *Journal of the European Ceramic Society* 39 (2019): 115–143, https://doi.org/10.1016/j.jeurceramsoc.2018.08.048.

26. K. Terauds, J.-M. Lebrun, H.-H. Lee, et al., "Electroluminescence and the Measurement of Temperature During Stage III of Flash Sintering Experiments," *Journal of the European Ceramic Society* 35 (2015): 3195–3199, https://doi.org/10.1016/j.jeurceramsoc.2015.03.040.

27. T. P. Mishra, C. Lenser, R. Raj, O. Guillon, and M. Bram, "Development of a Processing Map for Safe Flash Sintering of Gadolinium-Doped Ceria," *Journal of the American Ceramic Society* 104 (2021): 4316–4328, https://doi.org/10.1111/jace.17847.

28. Ü. Özgür, C. L. Ya.I. Alivov, A. Teke, et al., "A Comprehensive Review of ZnO Materials and Devices," *Journal of Applied Physics* 98 (2005): 041301, https://doi.org/10.1063/1.1992666.

29. D. Lewin, K.-H. Menze, I. Michiels, and D. C. Lupascu, "Influence of Geometry on Thermal Gradients and Hotspot Formation during Flash Sintering," *Journal of the European Ceramic Society* 43 (2023): 1633–1638, https://doi.org/10.1016/j.jeurceramsoc.2022.11.016.

30. A. B. Djurišić and Y. H. Leung, "Optical Properties of ZnO Nanostructures," *Small* 2 (2006): 944–961, https://doi.org/10.1002/smll.200600134.

31. S. K. Misra, S. I. Andronenko, D. Tipikin, J. H. Freed, V. Somani, and O. Prakash, "Study of Paramagnetic Defect Centers in as-Grown and Annealed TiO_2 Anatase and Rutile Nanoparticles by a Variable-Temperature X-Band and High-Frequency (236GHz) EPR," *Journal of Magnetism and Magnetic Materials* 401 (2016): 495–505, https://doi.org/10.1016/j.jmmm.2015.10.072.

32. B. Matović, J. Maletaškić, S. Panda, et al., "Facile Synthesis and Pressureless Sintering of $AlPO_4$ Nanopowders via a Modified Ouzo Method: Microstructures and Thermal Properties," *Ceramics International* 52 (2026): 29642–29652, https://doi.org/10.1016/j.ceramint.2026.05.043.

33. M. Ju, J. Kim, and J. Shin, "EPR Spectroscopy: A Versatile Tool for Exploring Transition Metal Complexes in Organometallic and Bioinorganic Chemistry," *Bulletin of the Korean Chemical Society* 45 (2024): 835–862, https://doi.org/10.1002/bkcs.12899.

34. S. B. Hong, S. J. Kim, and Y. S. Uh, "Fundamental Defect Centers in $AlPO_4$-5 and VPI-5 Molecular Sieves," *Journal of Physical Chemistry* 100 (1996): 15923–15925, https://doi.org/10.1021/jp961275x.

35. S. R. Teeparthi, E. W. Awin, and R. Kumar, "Dominating Role of Crystal Structure Over Defect Chemistry in Black and White Zirconia on Visible Light Photocatalytic Activity," *Scientific Reports* 8 (2018): 5541, https://doi.org/10.1038/s41598-018-23648-0.

36. R. Al-Gaashani, S. Radiman, A. R. Daud, N. Tabet, and Y. Al-Douri, "XPS and Optical Studies of Different Morphologies of ZnO Nanostructures Prepared by Microwave Methods," *Ceramics International* 39 (2013): 2283–2292, https://doi.org/10.1016/j.ceramint.2012.08.075.

37. V. Mishra, X. Vendrell, G. A. Faria, S. Bhat, R. Kumar, and D. Yadav, "Separating Thermally and Athermally Generated Lattice Strain During Flash Sintering," *Scripta Materialia* 285 (2026): 117515, https://doi.org/10.1016/j.scriptamat.2026.117515.

38. C. Queiroz, R. Carvalho, and F. Moura, "Oxidation of Zinc Sulphide Concentrate in a Fluidised Bed Reactor - Part 2: The Influence of Experimental Variables on the Kinetics," *Brazilian Journal of Chemical Engineering* 22 (2005): 127–133, https://doi.org/10.1590/S0104-66322005000100013.

39. T. K. Gupta and R. L. Coble, "Sintering of ZnO: I, Densification and Grain Growth," *Journal of the American Ceramic Society* 51 (1968): 521–525, https://doi.org/10.1111/j.1151-2916.1968.tb15679.x.

40. K. J. Cannon and K. G. Denbigh, "Studies on Gas-Solid Reactions—I: The Oxidation Rate of Zinc Sulphide," *Chemical Engineering Science* 6 (1957): 145–154, https://doi.org/10.1016/0009-2509(57)85013-1.

41. T. Rosenqvist, *Principles of Extractive Metallurgy* (Tapir Academic Press, 2004).

42. B. Yoon, D. Yadav, S. Ghose, P. Sarin, and R. Raj, "On the Synchronicity of Flash Sintering and Phase Transformation," *Journal of the American Ceramic Society* 102 (2019): 3110–3116, https://doi.org/10.1111/jace.16335.

43. M. K. P. Kumar, D. Yadav, J.-M. Lebrun, and R. Raj, "Flash Sintering With Current Rate: A Different Approach," *Journal of the American Ceramic Society* 102 (2019): 823–835, https://doi.org/10.1111/jace.16037.

15272648, 0, Downloaded from https://advanced.onlinelibrary.wiley.com/doi/10.1002/adem.71296 by Central Library The Librarian, Wiley Online Library on [11/10/2026]. See the Terms and Conditions (https://onlinelibrary.wiley.com/terms-and-conditions) on Wiley Online Library for rules of use; OA articles are governed by the applicable Creative Commons License

44. P. Rai and D. Yadav, "A First Study on the Current-Controlled Flash Sintering Experiments on 3YSZ-Ni Composites for SOFC Anode Applications," *Materials Chemistry and Physics* 316 (2024): 129088, https://doi.org/10.1016/j.matchemphys.2024.129088.

45. K. S. Arya, A. K. Kalyani, and T. Chakrabarti, "Flash Sintering of Lead Zirconate Titanate (PZT) With Minimal Lead Oxide Loss and Enhanced Dielectric Properties," *Journal of the European Ceramic Society* 44 (2024): 2797–2810, https://doi.org/10.1016/j.jeurceramsoc.2023.11.067.

46. B. Reeja-Jayan and J. Luo, "Far-From-Equilibrium Effects of Electric and Electromagnetic Fields in Ceramics Synthesis and Processing," *MRS Bulletin* 46 (2021): 26–35, https://doi.org/10.1557/s43577-020-00009-9.

47. H. Yamamoto, S. Tanaka, and K. Hirao, "Effects of Substrate Temperature on Nanostructure and Band Structure of Sputtered Co_3O_4 Thin Films," *Journal of Applied Physics* 93 (2003): 4158–4162, https://doi.org/10.1063/1.1555681.

48. L. Soriano, M. Abbate, J. Vogel, et al., "The Electronic Structure of Mesoscopic NiO Particles," *Chemical Physics Letters* 208 (1993): 460–464, https://doi.org/10.1016/0009-2614(93)87173-Z.

49. K. C. Sharma and Y. A. Chang, "The S-Zn (Sulfur-Zinc) System," *Journal of Phase Equilibria* 17 (1996): 261–266, https://doi.org/10.1007/BF02648496.

50. B. Yoon, D. Yadav, R. Raj, et al., "Measurement of O and Ti Atom Displacements in TiO_2 During Flash Sintering Experiments," *Journal of the American Ceramic Society* 101 (2018): 1811–1817, https://doi.org/10.1111/jace.15375.

51. W. Rheinheimer, X. L. Phuah, H. Wang, F. Lemke, M. Hoffmann, and H. Wang, "The Role of Point Defects and Defect Gradients in Flash Sintering of Perovskite Oxides," *Acta Materialia* 165 (2008): 398–408, https://doi.org/10.1016/j.actamat.2018.12.007.

52. D. Kok, D. Yadav, E. Sortino, et al., "α-Alumina and Spinel React Into Single-Phase High-Alumina Spinel in <3 seconds During Flash Sintering," *Journal of the American Ceramic Society* 102 (2019): 644–653, https://doi.org/10.1111/jace.15927.

53. T. Tian, L. Cheng, L. Zheng, et al., "Defect Engineering for a Markedly Increased Electrical Conductivity and Power Factor in Doped ZnO Ceramic," *Acta Materialia* 119 (2016): 136–144, https://doi.org/10.1016/j.actamat.2016.08.026.

54. X. Chen, G. Li, T. Tian, et al., "Microstructural and Electrical Features of Highly Conducting Indium Co-Doped ZnO-Based Ceramics," *Journal of the American Ceramic Society* 105 (2022): 6680–6692, https://doi.org/10.1111/jace.18633.

55. C. P. Singh, V. P. Singh, H. Ranjan, and S. K. Pandey, "Investigation of Resistive Switching Dynamics in E-Beam Evaporated P-Type Tin-Oxide Based Cross-Cell Memristor for Synaptic and Memory Application," *Materials Letters* 352 (2023): 135156, https://doi.org/10.1016/j.matlet.2023.135156.

56. C. Hu, Q. Wang, S. Bai, et al., "The Effect of Oxygen Vacancy on Switching Mechanism of ZnO Resistive Switching Memory," *Applied Physics Letters* 110 (2017): 073501, https://doi.org/10.1063/1.4976512.

Supporting Information

Additional supporting information can be found online in the Supporting Information section.

15272648, 0, Downloaded from https://advanced.onlinelibrary.wiley.com/doi/10.1002/adem.71296 by Central Library The Librarian, Wiley Online Library on [11/10/2026]. See the Terms and Conditions (https://onlinelibrary.wiley.com/terms-and-conditions) on Wiley Online Library for rules of use; OA articles are governed by the applicable Creative Commons License